ACSNANO

www.acsnano.org

ARTICLE

Size-Controlled Intercalation-to-Conversion Transition in Lithiation of Transition-Metal Chalcogenides—$NbSe_3$

Langli Luo,[†] Benliang Zhao,[‡] Bin Xiang,*[,‡] and Chong-Min Wang*[,†]

[†]Environmental Molecular Sciences Laboratory, Pacific Northwest National Laboratory, 902 Battelle Boulevard, Richland, Washington 99352, United States

[‡]Department of Materials Science & Engineering, Chinese Academy of Sciences Key Laboratory of Materials for Energy Conversion, University of Science and Technology of China, 96 Jinzhai Road, Hefei, Anhui 230026, China

Supporting Information

ABSTRACT: **Transition-metal chalcogenides (TMCs) can be used either as intercalation cathodes or as conversion-type anodes for lithium ion batteries, for which two distinctively different lithiation reaction mechanisms govern the electrochemical performance of TMCs. However, the factors that control the transition of lithiation mechanisms remain elusive. In this work, we investigated the lithiation process of $NbSe_3$ ribbons using *in situ* transmission electron microscopy and observed a size-dependent transition from intercalation to the conversion reaction. Large $NbSe_3$ ribbons can accommodate high concentrations of Li^+ through intercalation by relaxing their internal spacing, while lithiation of small $NbSe_3$ ribbons proceeds readily to full conversion. We found that the size-dependent variation of the lithiation mechanism is associated with both Li^+ diffusion in $NbSe_3$ and the accommodation of newly formed phases. For large $NbSe_3$ ribbons, the intercalation-to-conversion transition is impeded by both long-range Li^+ diffusion and large-scale accommodation of volume expansion induced by the formation of new phases. These results demonstrate the inherent structural instability of $NbSe_3$ as an intercalation cathode and its high lithiation rate as a promising conversion-type anode.**

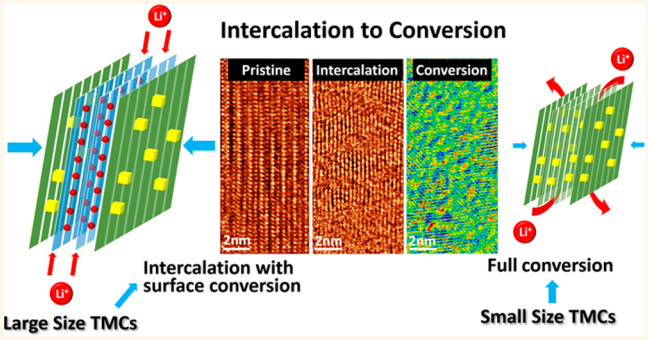

KEYWORDS: *transition-metal chalcogenides (TMCs), Li ion batteries, in situ TEM, $NbSe_3$, intercalation, conversion*

Transition-metal chalcogenides (TMCs) have been extensively investigated in recent years as catalysts for the hydrogen evolution reaction, high-performance electronics, and especially energy storage applications such as high-energy capacitors and lithium/magnesium ion batteries.[1−3] The layered or tunneled structures make TMCs a natural host to conveniently accommodate guest alkali ions such as Li^+ and Mg^+. Hence, TiS_2 and MoS_2 were chosen as intercalation cathode materials for lithium ion batteries (LIBs) in the early designs of rechargeable LIBs.[4,5] Similarly, TiS_3 and $NbSe_3$ were also studied as candidate cathodes for rechargeable LIBs until the 1990s.[6−10] Despite the exceptional performance of TMCs as cathode materials, the metal Li anode in the system consistently brought safety problems because of the growth of Li dendrites during the charge/discharge process.[11] Also, with the commercialization of $LiCoO_2$, $LiFePO_4$, $LiMn_2O_2$, and other high-voltage multimetal oxides as cathode materials, the exploration of TMCs has been largely deterred. Until recently, studies of nanostructured or few-layer transition-metal chalcogenides (TMCs) and their nanocomposites as conversion-type anodes for LIBs have been revived, largely encouraged by the discovery of graphene and other two-dimensional materials. MoS_2 nanoflakes,[12] nanoplates,[13] exfoliated and restacked MoS_2[14] and its nanocomposites,[15,16] and WS_2 and its nanocomposites[17,18] often exhibit specific capacities of 600−1100 mA h g^{-1}. Besides, TiS_2 and MoS_2 have been revisited as cathode materials for all-solid-state LIBs[19] and magnesium ion batteries.[20−22] It is expected that all TMCs with weak van der Waals interactions can be used as conversion anodes.

Despite numerous synthesis and electrochemical performance studies of layered TMCs, fundamental understanding of their lithiation mechanisms have rarely been explored.[23,24] Recently, a planar $LiMoS_2$ battery was investigated by an *in situ*

Received: October 20, 2015
Accepted: November 22, 2015
Published: November 23, 2015

DOI: 10.1021/acsnano.5b06614
ACS Nano 2016, 10, 1249−1255

method, revealing the effect of the lithiation process on the specific capacity and rate performance.[25] Also, the trigonal-prismatic (2H)-to-octahedral (1T) phase transition with a lithium ion occupying the interlayer S−S tetrahedral site has recently been directly observed during lithiation of MoS_2 nanosheets.[26] However, after 120 s the lithiated MoS_2 is converted to amorphous Li_2S. The weak van der Waals forces between layers enable hosting of guest ions between the layers or in the tunnels but also cause potential structural instability of the cathode matrix during the intercalation/extraction process. Recent first-principles calculations[27] show high Li^+ and Mg^+ mobility on TMC nanotubes, resulting in thermodynamically unstable structures upon ion insertion. Although these results show the structural changes of TMCs as an intercalation compound during Li^+ insertion, the ways that the layered or tunneled structures of TMCs change/degrade upon the Li^+ insertion and further react with Li^+ to achieve large capacities as conversion-type anodes are still unclear. In this work, we used *in situ* transmission electron microscopy (TEM) to investigate the structural and chemical changes of $NbSe_3$ ribbons upon lithiation. We have found that the $NbSe_3$ lithiation process is highly dependent on the size of the $NbSe_3$ ribbon: larger $NbSe_3$ ribbons (a few hundred nanometers in diameter) can host Li^+ through lattice distortion, while the lithiation of small $NbSe_3$ ribbons (<100 nm in width) proceeds quickly to the conversion reaction, represented by the formation of Li_2Se. This variation in the mechanism of $NbSe_3$ lithiation is attributed to the diffusion of Li^+ and the accommodation of volume expansion accompanied by the formation of new phases in the pristine nanostructures.

RESULTS AND DISCUSSION

$NbSe_3$ grows as ribbonlike crystals with each Nb atom at the center of a trigonal prism of Se atoms, which are arranged in chains along the *y* axis of the monoclinic structure. The chains are held together by quasi-van der Waals forces, similar to those in layered TMDs, which makes $NbSe_3$ a quasi-layered structure with layers made up of trigonal-prismatic chains. The scanning electron microscopy (SEM) image in Figure 1A shows the typical overall morphology of the $NbSe_3$ ribbon with a lateral size ranging from subhundred nanometers to a few microns. Figure 1B,C presents high-resolution TEM (HRTEM) and high-angle annular dark-field scanning TEM (HAADF-STEM)

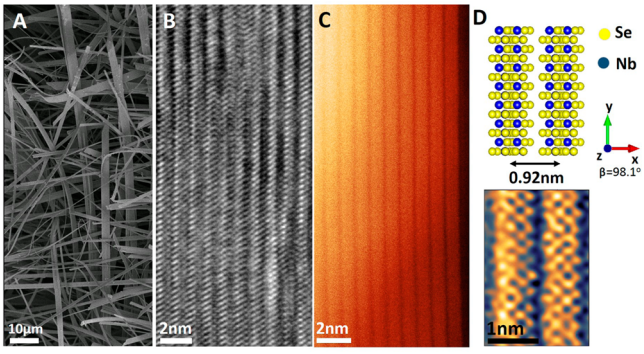

Figure 1. (A) SEM image of the overall morphology of $NbSe_3$ ribbons. (B) HRTEM and (C) HAADF-STEM images showing the chain structure of a $NbSe_3$ ribbon. (D) Schematic atomic structure of a $NbSe_3$ ribbon from the projected view along the *z* axis (upper) and an atomic-scale HAADF-STEM image (lower) revealing the chain structure of a pristine $NbSe_3$ ribbon.

images of the chain structure of $NbSe_3$, revealing the internal spacing for hosting Li^+. Figure 1D shows a schematic illustration of the crystal structure of $NbSe_3$ projected along the *z* axis (upper panel), matches well with the atomic structure revealed by the HR-HAADF image (lower panel). It is noted that the chain structure of $NbSe_3$ can be seen as a layered structure along the projection view along the *z* axis as shown in Figure 1C,D, and our observations are also based on this direction. The lithiation experiment was conducted using a nanobattery setup as illustrated in Figure S1. The $NbSe_3$ ribbons were loaded on a Pt tip and brought to contact with Li_2O-covered Li metal preloaded on a W tip inside the TEM chamber. A negative bias (−2 V) was applied on the Pt end, driving diffusion of Li^+ through the Li_2O (working as a solid electrolyte) to react with $NbSe_3$. On the contrary, the delithiation process was realized by applying a positive bias to $NbSe_3$.

Figure 2 shows a series of time-resolved bright-field TEM images captured from movie S1 (upper panel) and the

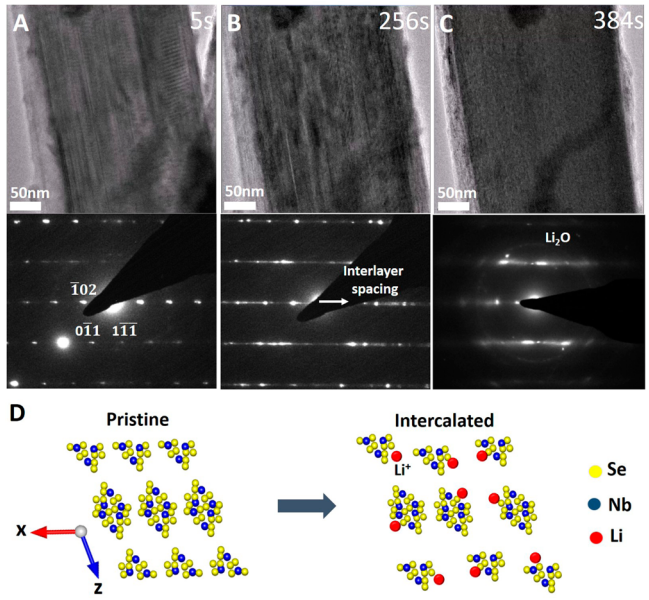

Figure 2. (A−C) Time-resolved TEM images and corresponding SAED patterns for the lithiation process of a large (~300 nm in width) $NbSe_3$ ribbon. (D) Schematic illustrations of pristine and intercalated $NbSe_3$ from the projection view along the *y* axis showing the expanded interchain spacing.

corresponding selected-area electron diffraction (SAED) patterns (lower panel) depicting the lithiation process of a $NbSe_3$ ribbon. Immediately after application of the bias, as shown in Figure 2A, the diffraction contrast of the chain structure of $NbSe_3$ changes and moiré fringes show up both parallel and perpendicular to the chain direction, which reflect the onset of strains caused by lattice expansion. After 256 s, the chain structure of $NbSe_3$ is still seen in the TEM image, but the SAED pattern in Figure 2B shows that diffraction spots elongate to form streaks along the direction perpendicular to the chains. This means that the interchain spacing varies from area to area along the chains while the atomic structure in each chain is maintained, indicating heavy Li^+ intercalation and a strongly interacted surface of each chain. The diffraction contrast from the chain structure of the $NbSe_3$ ribbon has disappeared after ~300 s, and instead, a more uniform mass−

DOI: 10.1021/acsnano.5b06614
ACS Nano 2016, 10, 1249−1255

thickness contrast shows up on the $NbSe_3$ ribbon, as shown in Figure 2C. However, the corresponding SAED pattern still shows streaks, and the distance of the atomic planes in the y direction is maintained besides the emergence of Li_2O, indicating that the atomic structure of each chain is still intact. This lithiation process, illustrated in Figure 2D, causes an expansion of the interchain spacing in both the x and z directions while the atomic structure in the y direction remains unchanged, and it also causes sliding between chains. This lithiation process with expansion along only the x and z axes has been reported for Li intercalation of $NbSe_3$ up to $3Li^+$. Here we have shown that under a much larger driving force (−2 V), the lithiation of this $NbSe_3$ ribbon proceeds predominantly through an intercalation mechanism with most of the chain structure retained.

To further elucidate the structure of lithiated $NbSe_3$, we found a ribbon with a thin edge, as shown in the STEM-HAADF image in Figure 3A, which was lithiated for a few minutes. The TEM image in Figure 3B shows distinctive contrast for regions from the surface to the center of the lithiated $NbSe_3$ ribbon. In the enlarged view in Figure 3C, three regions are marked by the white dashed lines. The outermost region (~10 nm in width) corresponds to the surface Li_2O formed by the excess supply of Li^+ on the surface of ribbon, which also was shown in the SAED pattern in Figure 2D. The intermediate region (~20 nm in width) and inner region were further examined by the HRTEM images in Figure 3D,E. The square lattice in Figure 3D is well-matched with the face-centered cubic structure of Li_2Se, which confirms that the conversion reaction took place in the region near the surface. The inner region of the lithiated $NbSe_3$ ribbon shows obvious changes from the pristine $NbSe_3$ structure but still maintains the chain structure, as evidenced by HRTEM image in Figure 3E, which is in accordance with the SAED patterns in Figure 2B,C showing the preserved crystal structure of $NbSe_3$. This observation indicates that the large inner region of this $NbSe_3$ ribbon is the intercalation region, where Li^+ ions are well-accommodated among the chains by relaxation of the interchain spacing. The above results show that the lithiation of $NbSe_3$ ribbons with a lateral dimension of a few hundred nanometers results in a conversion reaction in the surface region but intercalation in the majority of the inner region of the ribbon. This variation of the lithiation reaction mechanism between the surface and inner bulk regions of $NbSe_3$ ribbons implies a possible effect of size on the lithiation behavior of TMC nanostructures since the size of the nanostructure can change the surface-to-volume ratio significantly, which may lead to distinctive lithiation behavior. This hypothesis is supported by the following experimental observations.

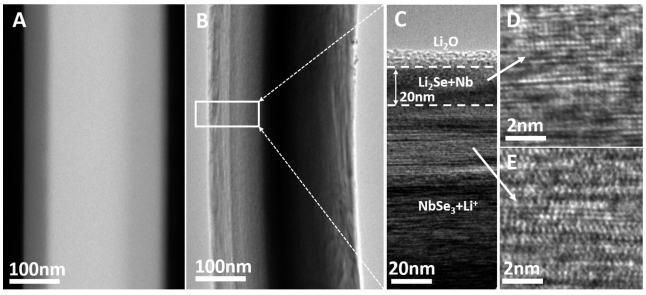

Figure 3. (A) HAADF-STEM image of a pristine $NbSe_3$ ribbon with a thin edge. (B) TEM image of the lithiated $NbSe_3$ ribbon. (C) Enlarged area from the white box in (B). The distinct regions from the edge to the center of the $NbSe_3$ ribbon are shown by the white dashed lines. (D, E) HRTEM images from two of the regions in (C).

We also examined the lithiation process of a much smaller $NbSe_3$ ribbon with dimensions of ~326.8 nm × 50.2 nm (Figure 4A). The lithiation of this ribbon proceeded extremely fast and was essentially complete within a few seconds. The lithiated ribbon expanded from 50.2 to 133.3 nm laterally, as shown in Figure 4B. This was mostly due to the unfolding of the ribbons, and the chain structure was fully converted to a nanocomposite structure of small nanoparticles embedded in a matrix, which is a typical structure for conversion-type anode materials after lithiation.[28,29] The HAADF-STEM image in Figure 4C shows that the matrix lattice matches well with that of $Li_2Se(111)$, and the dispersed nanoparticles are Nb metal nanoparticles with a bright contrast (white dashed circles). The

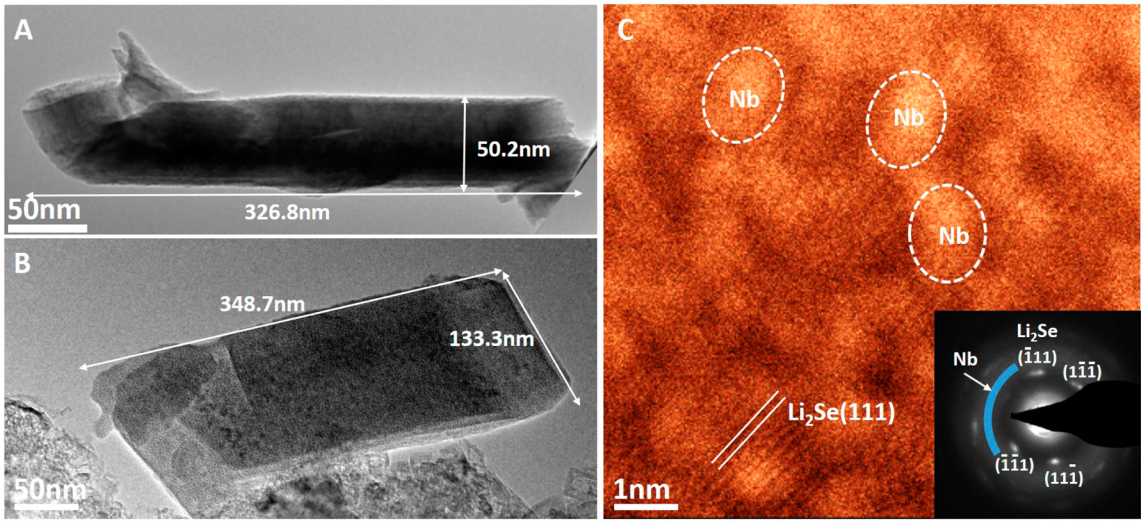

Figure 4. (A, B) TEM images of a small (A) pristine and (B) lithiated $NbSe_3$ ribbon. (C) HAADF-STEM images of the lithiated $NbSe_3$ ribbon showing the Nb metal particles embedded in the Li_2Se matrix. The inset is the corresponding SAED pattern.

DOI: 10.1021/acsnano.5b06614
ACS Nano 2016, 10, 1249−1255

inset of Figure 4C shows the SAED pattern of the lithiated ribbon, which confirms the presence of Nb metal nanoparticles by the diffusing ring and the Li_2Se phase by the labeled diffraction spots. The above observations reveal that a small $NbSe_3$ ribbon can go through the full conversion reaction $NbSe_3 + 6Li^+ + 6e^- \rightarrow Nb + 3Li_2Se$ quickly without an observable intercalation process and intermediate product. The high conversion rate is related to the excellent Li^+ and electron conductivities of $NbSe_3$. Along with the observation of intercalation with surface conversion for large $NbSe_3$ ribbons, we see an obvious size-dependent lithiation mechanism for $NbSe_3$, and it is reasonable to speculate that this effect could also be applied to other van der Waals TMCs, although the critical size for the intercalation-to-conversion transition may vary for different materials. For the case of delithiation of the converted material, the structure was also observed using HRTEM, as representatively illustrated in Figure S2. However, the delithiation products appear to be very complicated, and it is hard to conclusively determine the structure of the delithiated phase. Therefore, more detailed work must be done regarding the delithiation mechanism within the current system.

This size-dependent lithiation mechanism observed for $NbSe_3$ can be understood from both chemical and mechanical aspects. Chemically, the lithiation reaction of $NbSe_3$ is determined by both thermodynamic and kinetic factors. The kinetic factors such as diffusion of Li^+ in the $NbSe_3$ ribbon and the nucleation of new phases (Nb, Li_2Se) predominate while the electrochemical potential (the applied bias) of the reaction is kept the same in the above experiments. The size of the $NbSe_3$ ribbons affects the lithiation kinetics in the following two ways. First, the $NbSe_3$ ribbon with smaller size has a much larger surface-to-volume ratio, resulting in a much larger fraction of surface reaction with Li^+. The lithiation rate on the surface of the ribbon is always higher than that in the bulk because the surface of the $NbSe_3$ ribbon is always saturated with Li^+ first upon lithiation. Second, Li^+ diffusion in the bulk of $NbSe_3$ is also facilitated by the smaller size of the $NbSe_3$ ribbon. It is known that diffusion of Li^+ across chains is much more difficult than diffusion through the interchain spacing. When Li^+ ions diffuse through the interchain spacing, the first ones always end up anchored on sites close to the entrance (surface) of the ribbon, and the later Li^+ ions have to move forward to the inner area. With a shorter diffusion distance, the conversion reaction on the surface of ribbons can quickly propagate into the bulk easily because of the short diffusion length, as shown in Figure 4. We know that the product of the conversion reaction for $NbSe_3$ is a nanocomposite of the Li_2Se matrix embedded with Nb nanoparticles and that it is neither a good Li^+ conductor nor a good electron conductor, which requires a short diffusion length for the continuing conversion reaction. Hence, the enhanced Li^+ diffusion in the $NbSe_3$ ribbon with smaller size facilitates the conversion reaction, while in the $NbSe_3$ ribbon with larger size only the surface region is converted.

The effect of size on the lithium diffusion conditions discussed above also implies that we can change the local chemical condition of $NbSe_3$ to change the critical size of the intercalation-to-conversion transition. To verify this point, we intentionally chose a small $NbSe_3$ ribbon (~50 nm in diameter) attached to a much bigger ribbon (>200 nm in diameter), which lowered the electrochemical potential on the small $NbSe_3$ ribbon, leading to a limited Li^+ diffusion environment for this ribbon. As shown in the time-resolved TEM images in Figure 5A–C, this $NbSe_3$ ribbon experiences an intercalation process similar to that depicted in Figure 2A–C in 25 min with

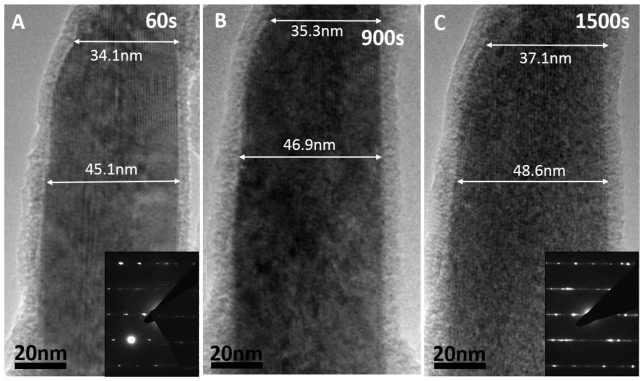

Figure 5. Time-resolved TEM images and corresponding SAED patterns of the lithiation process of a small $NbSe_3$ ribbon (~45 nm in width) attached to a much bigger ribbon, which shows only intercalation under limited Li diffusion conditions.

a measured expansion of ~8% in width. The corresponding SAED patterns shown in the insets of Figure 5A,C confirm that the interchain spacing changes while the atoms within the chains remain in their original structure, which is also similar to the observations in Figure 2. Apparently, the limited Li^+ diffusion environment prevents the $NbSe_3$ ribbon from being converted for a much longer period of time, which confirms that the critical size for the intercalation-to-conversion transition can be changed by local chemical variation.

Mechanically, the conversion-reaction-induced volume expansion also impedes the conversion reaction, leading to the surface-only conversion reaction for large-sized $NbSe_3$ ribbons. To understand this retardation effect, it is always intriguing to see how the pristine chain structure is destroyed mechanically and how the new phase nucleates and takes the place of the pristine structure. This process is illustrated at the atomic scale for the first time for a $NbSe_3$ ribbon with a lateral dimension of ~16 nm (~50 layers), as shown in a series of time-resolved HRTEM images (Figure 6) captured from movie S2. In Figure 6A, the diffraction contrast of straight lines shows the chain structure of this $NbSe_3$ ribbon, and we see a few segments of $NbSe_3$ with a thickness of 8–10 layers and a length of ~5 nm embedded in a matrix in the lower-right protruding area. These segments were possibly stripped from the $NbSe_3$ ribbon on the left before our observation. It is also noted that the defects on the $NbSe_3$ ribbon indicated by the two black arrows are present, where the conversion reaction initiates later. For the area indicated by the black arrow at the bottom, a few layers of $NbSe_3$ are stripped from the $NbSe_3$ ribbon through attack at the defect location. After 374 s, a large segment of $NbSe_3$ indicated by white dashed ellipse in Figure 6B starts to become isolated from the ribbon, and the two ends of this segment are the two defect locations previously identified by the black arrows in Figure 6A. After 620 s (Figure 6C), the chain structure of small segments of $NbSe_3$ in the lower-right protruding area disappears, indicating that they have been fully converted. In addition, the isolated larger $NbSe_3$ segment indicated by white dashed ellipse shrinks in size from 19.2 to 12.1 nm and the thickness decreases from 10 to 6 layers, also indicating that this $NbSe_3$ segment is converted gradually. In Figure 6D, the absence of most of the diffraction contrast of

DOI: 10.1021/acsnano.5b06614
ACS Nano 2016, 10, 1249–1255

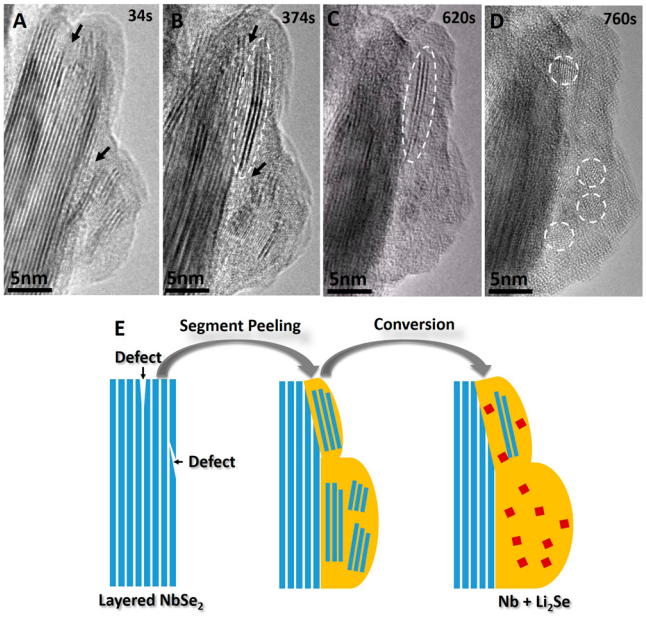

Figure 6. (A–D) Time-resolved TEM images depicting the lithiation process of a $NbSe_3$ ribbon (~20 nm in width) attached to a much bigger ribbon, which shows the breaking of the layered structure leading to an intercalation-to-conversion transition under controlled Li diffusion conditions. (E) Schematic illustration of this lithiation showing a segment peeling and conversion process.

straight lines and the emergence of small crystal particles, indicated by white dashed circles, indicate that the conversion reaction largely proceeded through this area. The above observations show that the conversion reaction of $NbSe_3$ is initiated from the sites of defects on the pristine ribbon, after which segment-by-segment peeling and conversion occur, as illustrated in Figure 6E. In this way, the nucleated new phases can be accommodated by a notable volume expansion, as shown in going from Figure 6A to Figure 6D. This process apparently takes place more easily for small $NbSe_3$ ribbons than larger ones because the former have a large surface-to-volume ratio with more surface defects exposed. For larger $NbSe_3$ ribbons, it is hard for new phases to nucleate in the limited spacing of layered structures. Moreover, as the conversion reaction proceeds, stress can be generated by the volume expansion in the unreacted area, which retards and/or halts the conversion reaction, leading to a ribbon converted only on the surface with most of its layered structure maintained, as shown in Figure 3. Figure 7 schematically illustrates the effect of the size of the $NbSe_3$ ribbon on the lithiation mechanism and highlights that the observed size effect is related to Li^+ diffusion and mechanical confinement. Apparently, regardless of the length or the thickness of the ribbon, intercalation can readily happen. However, because of the diffusion and mechanical confinement for conversion, a longer ribbon can be converted only if it is a thin one. In more general terms, what has been observed regarding the size effect based on $NbSe_3$ can be extended to other van der Waals TMCs, but the critical size of the intercalation-to-conversion transition can be different for different TMCs. For morphologies other than ribbons, the general principle of the diffusion-limited and mechanical confinement effect on the intercalation-to-conversion transition will still hold true.

We finally discuss the role of van der Waals TMCs as electrodes in Li or other alkali-metal-based batteries. As a cathode material, van der Waals TMCs are not structurally as stable as current cathode materials (e.g., $LiCoO_2$, $LiMn_2O_2$, and $LiPO_4$) since they can electrochemically react with Li. Although the conversion reaction is mostly limited to the surface for van der Waals TMCs with larger size, the converted surface area can inhibit Li^+ and electron transport during subsequent cycling of the battery. However, as an anode material, smaller-sized van der Waals TMCs have higher lithiation rates, and more complete reversible conversion can be reached.

CONCLUSIONS

We have investigated the electrochemical lithiation mechanism of the van der Waals TMC $NbSe_3$. A size-dependent reaction mechanism has been found, featuring a full conversion reaction for smaller-sized $NbSe_3$ ribbons, while the conversion reaction

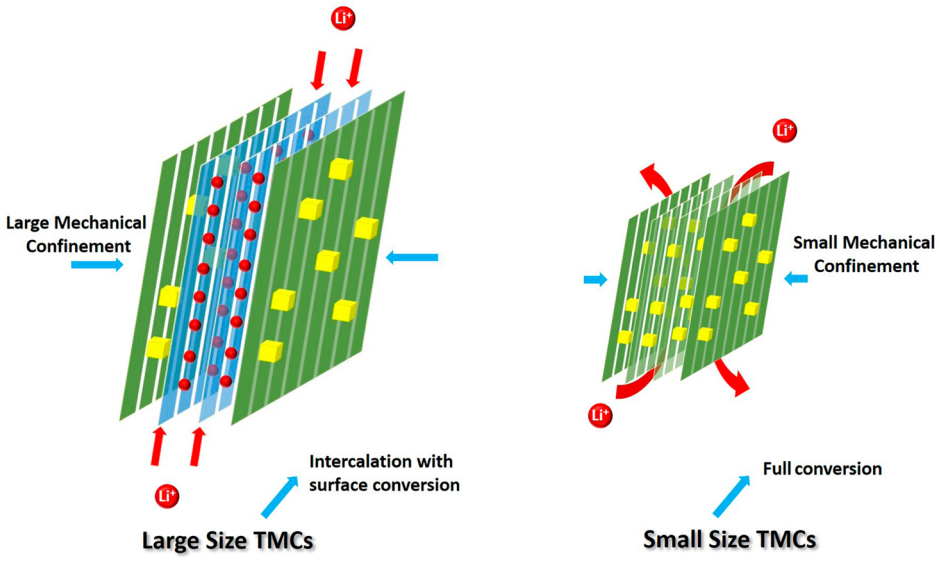

Figure 7. Schematic illustration of the effect of size on the lithiation reaction mechanism: the large-sized TMC is dominated by intercalation and the surface region is subjected to the conversion reaction, whereas the small-sized TMC is fully converted upon lithiation.

DOI: 10.1021/acsnano.5b06614
ACS Nano 2016, 10, 1249–1255

takes place only on the surface of larger $NbSe_3$ ribbons with most of the inner part of the ribbon intercalated with Li^+. The observed dependence of the lithiation mechanism on the size of the $NbSe_3$ ribbon is attributed to the size-associated Li^+ diffusion and mechanical confinement effect. The critical size for this intercalation-to-conversion transition can be changed by modifying the local chemical potential and diffusion conditions. These fundamental observations of the lithiation mechanism provide guidance for the rational design of electrode systems for high-capacity, high-performance Li ion batteries.

METHODS

$NbSe_3$ ribbons were synthesized by a solid-phase reaction. Niobium powder (99.5% purity, Sinopharm Chemical Reagent Co., Ltd.) and selenium powder (99% purity, Sinopharm) with a mole ratio of 1:3 were utilized as the reactants. A precleaned quartz tube with a diameter of 5 mm was used as a reactor. After the reactants were loaded into the tube, it was sealed in an argon atmosphere. Subsequently, the sealed quartz tube was heated to 700 °C at a heating rate of 50 °C/min, and then the temperature was maintained for half an hour. As it was cooled to room temperature in a natural cooling process, $NbSe_3$ was obtained in the quartz tube.

STEM images of pristine $NbSe_3$ ribbons were collected on an FEI TITAN 80-300 S/TEM microscope with a probe aberration corrector using a HAADF detector. SEM images were obtained on a JEOL JSM-6700F field-emission scanning electron microscope. The *in situ* TEM observation of lithiation of $NbSe_3$ ribbons was performed on an FEI ETEM instrument with an objective-lens aberration corrector using a Nanofactory electrical probe holder. This holder has a dual-probe design, i.e., one Pt rod was loaded with $NbSe_3$ ribbons while a tungsten tip driven by a piezoelectric motor capable of 3D positioning with a step size of 1 nm was loaded with Li metal. The Li metal was covered with a thin layer of Li_2O by a few seconds of exposure to air during sample processing; the Li_2O acted as a solid electrolyte. The electrochemical lithiation was realized by connecting the two probes inside the TEM chamber. When a negative bias (−2 V) was applied to the Pt probe with the $NbSe_3$ ribbons, the Li ions were driven across the Li_2O to react with $NbSe_3$. We chose $NbSe_3$ because it can grow longer with a larger lateral size (with more stacking layers), which was suitable for testing our hypothesis of a size-controlled intercalation-to-conversion transition; other TMCs such as MoS_2 are usually synthesized with only a few layers and limited lateral size. At the same time, $NbSe_3$ has better electrical conductivity than most of the other TMCs, which was preferred in our nanobattery experimental settings.

ASSOCIATED CONTENT

Supporting Information

The Supporting Information is available free of charge on the ACS Publications website at DOI: 10.1021/acsnano.5b06614.

Figures S1 and S2 (PDF)

Movie showing the electrochemical lithiation of a $NbSe_3$ nanoribbon to illustrate the intercalation process (AVI)

Movie showing the electrochemical lithiation of a small $NbSe_3$ nanoribbon (~20 nm in diameter) attached to a bigger $NbSe_3$ to illustrate the intercalation-to-conversion transition (AVI)

AUTHOR INFORMATION

Corresponding Authors

*E-mail: binxiang@ustc.edu.cn.

*E-mail: Chongmin.Wang@pnnl.gov.

Notes

The authors declare no competing financial interest.

ACKNOWLEDGMENTS

This work at Pacific Northwest National Laboratory (PNNL) was supported by the Assistant Secretary for Energy Efficiency and Renewable Energy, Office of Vehicle Technologies, U.S. Department of Energy (DOE), under Contracts DE-AC02-05CH11231, Subcontract 18769, and DE-AC-36-08GO28308 under the Advanced Batteries Materials Research (BMR) Program. The *in situ* microscopic study described in this paper was supported by the Laboratory Directed Research and Development Program as part of the Chemical Imaging Initiative at PNNL. The work was conducted in the William R. Wiley Environmental Molecular Sciences Laboratory (EMSL), a National Scientific User Facility sponsored by DOE's Office of Biological and Environmental Research and located at PNNL. PNNL is operated by Battelle for the DOE under Contract DE-AC05-76RLO1830. B.X. acknowledges support from the National Natural Science Foundation of China (21373196).

REFERENCES

(1) Chhowalla, M.; Shin, H. S.; Eda, G.; Li, L.-J.; Loh, K. P.; Zhang, H. The Chemistry of Two-Dimensional Layered Transition Metal Dichalcogenide Nanosheets. *Nat. Chem.* **2013**, *5*, 263−275.

(2) Pumera, M.; Sofer, Z.; Ambrosi, A. Layered Transition Metal Dichalcogenides for Electrochemical Energy Generation and Storage. *J. Mater. Chem. A* **2014**, *2*, 8981−8987.

(3) Wang, H.; Feng, H.; Li, J. Graphene and Graphene-Like Layered Transition Metal Dichalcogenides in Energy Conversion and Storage. *Small* **2014**, *10*, 2165−2181.

(4) Whittingham, M. S. Lithium Batteries and Cathode Materials. *Chem. Rev.* **2004**, *104*, 4271−4302.

(5) Py, M. A.; Haering, R. R. Structural Destabilization Induced by Lithium Intercalation in MoS_2 and Related Compounds. *Can. J. Phys.* **1983**, *61*, 76−84.

(6) Chianelli, R. R.; Dines, M. B. Reaction of Butyllithium with Transition Metal Trichalcogenides. *Inorg. Chem.* **1975**, *14*, 2417−2421.

(7) Murphy, D. W.; Trumbore, F. A. The Chemistry of TiS_3 and $NbSe_3$ Cathodes. *J. Electrochem. Soc.* **1976**, *123*, 960−964.

(8) Ōnuki, Y.; Inada, R.; Tanuma, S.; Yamanaka, S.; Kamimura, H. Electrochemical Characteristics of Transition-Metal Trichalcogenides in the Secondary Lithium Battery. *Solid State Ionics* **1983**, *11*, 195−201.

(9) Scott, R. A.; Jacobson, A. J.; Chianelli, R. R.; Pan, W. H.; Stiefel, E. I.; Hodgson, K. O.; Cramer, S. P. Reactions of Molybdenum Trisulfide, Tungsten Trisulfide, Tungsten Triselenide, and Niobium Triselenide with Lithium. Metal Cluster Rearrangement Revealed by EXAFS. *Inorg. Chem.* **1986**, *25*, 1461−1466.

(10) Ratnakumar, B. V.; Nagasubramanian, G.; Di Stefano, S.; Bankston, C. P. Kinetics of Intercalation of Lithium into $NbSe_3$ and TiS_2 Cathodes. *J. Electrochem. Soc.* **1992**, *139*, 1513−1521.

(11) Tarascon, J. M.; Armand, M. Issues and Challenges Facing Rechargeable Lithium Batteries. *Nature* **2001**, *414*, 359−367.

(12) Dominko, R.; Arčon, D.; Mrzel, A.; Zorko, A.; Cevc, P.; Venturini, P.; Gaberscek, M.; Remskar, M.; Mihailovic, D. Dichalcogenide Nanotube Electrodes for Li-Ion Batteries. *Adv. Mater.* **2002**, *14*, 1531−1534.

(13) Hwang, H.; Kim, H.; Cho, J. MoS_2 Nanoplates Consisting of Disordered Graphene-like Layers for High Rate Lithium Battery Anode Materials. *Nano Lett.* **2011**, *11*, 4826−4830.

(14) Du, G.; Guo, Z.; Wang, S.; Zeng, R.; Chen, Z.; Liu, H. Superior Stability and High Capacity of Restacked Molybdenum Disulfide as Anode Material for Lithium Ion Batteries. *Chem. Commun.* **2010**, *46*, 1106−1108.

(15) Chang, K.; Chen, W. l-Cysteine-Assisted Synthesis of Layered MoS_2/Graphene Composites with Excellent Electrochemical Performances for Lithium Ion Batteries. *ACS Nano* **2011**, *5*, 4720−4728.

DOI: 10.1021/acsnano.5b06614
ACS Nano 2016, 10, 1249−1255

(16) Stephenson, T.; Li, Z.; Olsen, B.; Mitlin, D. Lithium Ion Battery Applications of Molybdenum Disulfide (MoS_2) Nanocomposites. *Energy Environ. Sci.* **2014**, *7*, 209−231.
(17) Bhandavat, R.; David, L.; Singh, G. Synthesis of Surface-Functionalized WS_2 Nanosheets and Performance as Li-Ion Battery Anodes. *J. Phys. Chem. Lett.* **2012**, *3*, 1523−1530.
(18) Shiva, K.; Ramakrishna Matte, H. S. S.; Rajendra, H. B.; Bhattacharyya, A. J.; Rao, C. N. R. Employing Synergistic Interactions between Few-Layer WS_2 and Reduced Graphene Oxide to Improve Lithium Storage, Cyclability and Rate Capability of Li-Ion Batteries. *Nano Energy* **2013**, *2*, 787−793.
(19) Trevey, J. E.; Stoldt, C. R.; Lee, S.-H. High Power Nanocomposite TiS_2 Cathodes for All-Solid-State Lithium Batteries. *J. Electrochem. Soc.* **2011**, *158*, A1282−A1289.
(20) Liang, Y.; Feng, R.; Yang, S.; Ma, H.; Liang, J.; Chen, J. Rechargeable Mg Batteries with Graphene-Like MoS_2 Cathode and Ultrasmall Mg Nanoparticle Anode. *Adv. Mater.* **2011**, *23*, 640−643.
(21) Tao, Y. R.; Xiong, W. W.; Wu, X. C. Titanium Tri- and Di-Sulfide Nanobelts/Graphene Composites for Rechargeable Lithium Battery Cathodes and Enhancement of Reversible Capacities. *Sci. Adv. Mater.* **2014**, *6*, 1965−1972.
(22) Liang, Y.; Yoo, H. D.; Li, Y.; Shuai, J.; Calderon, H. A.; Robles Hernandez, F. C.; Grabow, L. C.; Yao, Y. Interlayer-Expanded Molybdenum Disulfide Nanocomposites for Electrochemical Magnesium Storage. *Nano Lett.* **2015**, *15*, 2194−2202.
(23) Feng, C.; Ma, J.; Li, H.; Zeng, R.; Guo, Z.; Liu, H. Synthesis of Molybdenum Disulfide (MoS_2) for Lithium Ion Battery Applications. *Mater. Res. Bull.* **2009**, *44*, 1811−1815.
(24) Zeng, Z.; Sun, T.; Zhu, J.; Huang, X.; Yin, Z.; Lu, G.; Fan, Z.; Yan, Q.; Hng, H. H.; Zhang, H. An Effective Method for the Fabrication of Few-Layer-Thick Inorganic Nanosheets. *Angew. Chem., Int. Ed.* **2012**, *51*, 9052−9056.
(25) Wan, J.; Bao, W.; Liu, Y.; Dai, J.; Shen, F.; Zhou, L.; Cai, X.; Urban, D.; Li, Y.; Jungjohann, K.; Fuhrer, M. S.; Hu, L. *In Situ* Investigations of Li-MoS_2 with Planar Batteries. *Adv. Energy Mater.* **2015**, *5*, 1401742.
(26) Wang, L.; Xu, Z.; Wang, W.; Bai, X. Atomic Mechanism of Dynamic Electrochemical Lithiation Processes of MoS_2 Nanosheets. *J. Am. Chem. Soc.* **2014**, *136*, 6693−6697.
(27) Pereira, A. O.; Miranda, C. R. First-Principles Investigation of Transition Metal Dichalcogenide Nanotubes for Li and Mg Ion Battery Applications. *J. Phys. Chem. C* **2015**, *119*, 4302−4311.
(28) Wang, F.; Robert, R.; Chernova, N. A.; Pereira, N.; Omenya, F.; Badway, F.; Hua, X.; Ruotolo, M.; Zhang, R.; Wu, L.; et al. Conversion Reaction Mechanisms in Lithium Ion Batteries: Study of the Binary Metal Fluoride Electrodes. *J. Am. Chem. Soc.* **2011**, *133*, 18828−18836.
(29) Luo, L.; Wu, J.; Xu, J.; Dravid, V. P. Atomic Resolution Study of Reversible Conversion Reaction in Metal Oxide Electrodes for Lithium-Ion Battery. *ACS Nano* **2014**, *8*, 11560−11566.

DOI: 10.1021/acsnano.5b06614
ACS Nano 2016, 10, 1249−1255